Vol.51, Issue 1, January 2024, pp.509-521

Received: 27 March 2023 | Revised: 6 August 2023 | Accepted: 23 August 2023

DOI: 10.1002/mp.16727

RESEARCH ARTICLE

MEDICAL PHYSICS

Feasibility study of optical imaging of the boron-dose distribution by a liquid scintillator in a clinical boron neutron capture therapy field

Hideya Maeda[1] | **Akihiro Nohtomi**[1] | **Naonori Hu**[2,3] | **Ryo Kakino**[2] | **Kazuhiko Akita**[2] | **Koji Ono**[2]

[1]Graduate School of Medical Sciences, Kyushu University, Fukuoka-shi, Fukuoka, Japan

[2]Kansai BNCT Medical Center, Osaka Medical and Pharmaceutical University, Takatsuki-shi, Osaka, Japan

[3]Particle Radiation Oncology Research Center, Industrial Equipment Division, Kyoto University, Sennan-gun, Osaka, Japan

Correspondence
Akihiro Nohtomi, Graduate School of Medical Sciences, Kyushu University, 3-1-1, Maidashi, Higashi-ku, Fukuoka-shi, Fukuoka 812–8582, Japan.
Email: nohtomi.akihiro.858@m.kyushu-u.ac.jp

Abstract

Background: Evaluation of the boron dose is essential for boron neutron capture therapy (BNCT). Nevertheless, a direct evaluation method for the boron-dose distribution has not yet been established in the clinical BNCT field. To date, even in quality assurance (QA) measurements, the boron dose has been indirectly evaluated from the thermal neutron flux measured using the activation method with gold foil or wire and an assumed boron concentration in the QA procedure. Recently, we successfully conducted optical imaging of the boron-dose distribution using a cooled charge-coupled device (CCD) camera and a boron-added liquid scintillator at the E-3 port facility of the Kyoto University Research Reactor (KUR), which supplies an almost pure thermal neutron beam with very low gamma-ray contamination. However, in a clinical accelerator-based BNCT facility, there is a concern that the boron-dose distribution may not be accurately extracted because the unwanted luminescence intensity, which is irrelevant to the boron dose is expected to increase owing to the contamination of fast neutrons and gamma rays.

Purpose: The purpose of this research was to study the validity of a newly proposed method using a boron-added liquid scintillator and a cooled CCD camera to directly observe the boron-dose distribution in a clinical accelerator-based BNCT field.

Method: A liquid scintillator phantom with ^{10}B was prepared by filling a small quartz glass container with a commercial liquid scintillator and boron-containing material (trimethyl borate); its natural boron concentration was 1 wt%. Luminescence images of the boron-neutron capture reaction were obtained in a water tank at several different depths using a CCD camera. The contribution of background luminescence, mainly due to gamma rays, was removed by subtracting the luminescence images obtained using another sole liquid scintillator phantom (natural boron concentration of 0 wt%) at each corresponding depth, and a depth profile of the boron dose with several discrete points was obtained. The obtained depth profile was compared with that of calculated boron dose, and those of thermal neutron flux which were experimentally measured or calculated using a Monte Carlo code.

Results: The depth profile evaluated from the subtracted images indicated reasonable agreement with the calculated boron-dose profile and thermal neutron flux profiles, except for the shallow region. This discrepancy is thought to be due to the contribution of light reflected from the tank wall. The simulation results also demonstrated that the thermal neutron flux would be severely perturbed by the ^{10}B-containing phantom if a relatively larger container was

used to evaluate a wide range of boron-dose distributions in a single shot. This indicates a trade-off between the luminescence intensity of the ^{10}B-added phantom and its perturbation effect on the thermal neutron flux.

Conclusions: Although a partial discrepancy was observed, the validity of the newly proposed boron-dose evaluation method using liquid-scintillator phantoms with and without ^{10}B was experimentally confirmed in the neutron field of an accelerator-based clinical BNCT facility. However, this study has some limitations, including the trade-off problem stated above. Therefore, further studies are required to address these limitations.

KEYWORDS

boron neutron capture therapy (BNCT), boron-dose distribution, charge-coupled device (CCD), liquid scintillator, optical dosimetry, quality assurance (QA)

1 | INTRODUCTION

Boron neutron capture therapy (BNCT) uses the nuclear reaction of ^{10}B(n, α)^{7}Li, as expressed in Equation (1), to selectively kill tumor cells.[1] Following the reaction expressed in Equation (1), the excited state of the ^{7}Li nucleus (^{7}Li*) emits a prompt 478 keV gamma ray, as expressed in Equation (2).

$$^{10}B + n \rightarrow \begin{cases} ^{7}Li + \alpha\,(6\,\%,\ Q = 2.79\ MeV) \\ ^{7}Li^{*} + \alpha\,(94\,\%,\ Q = 2.31\ MeV) \end{cases} \quad (1)$$

$$^{7}Li^{*} \rightarrow {}^{7}Li + \gamma\,(478\ keV) \quad (2)$$

The physical dose deposited by ^{7}Li nuclei and alpha particles is known as the boron dose, and the treatment results of BNCT effectively depend on the boron dose. Hence, the direct measurement of boron-dose distribution is highly desirable for further progress in BNCT.

However, even in quality assurance (QA) measurements, the direct measurement of the boron-dose distribution has not yet been practically established owing to several technical difficulties. Thus far, only the thermal neutron flux distribution has been measured, and the boron-dose distribution has been indirectly evaluated by calculation from the measured thermal neutron flux by assuming an adequate boron concentration. For such thermal neutron flux measurements, a conventional activation method using a gold wire or foil is often used. The activation method is the most standard and reliable method; however, the measurement of multiple points using this method is time-consuming. Thus, in daily QA measurements, the activation method tends to be used for only a few limited point measurements.[2] For the further development of BNCT, it is desirable to establish a more convenient and dedicated method that can directly measure the boron-dose distribution.

The detection of the 478 keV prompt gamma rays emitted from ^{7}Li*, as expressed in Equation (2), is a promising candidate technique that enables the direct evaluation of boron concentration or boron dose in patients, because the number of 478 keV prompt gamma rays is proportional to the number of boron neutron capture reactions. Thus, several studies have been conducted to realize this method.[3–5] However, the reliable selective detection of 478 keV prompt gamma rays is difficult under severe background signals of 511 keV annihilation radiations owing to 2.2 MeV gamma rays emitted from the ^{1}H(n, γ)^{2}H reaction and under other intensive background gamma rays emitted from the neutron-originated process. Therefore, this method is still in the research phase, mainly because of the insufficient energy resolution and poor count-rate capability of the currently available detectors.

For BNCT dosimetry, several applications of gel detectors have also been studied because of their potential for three-dimensional (3D) dosimetry and the advantage of tissue equivalence.[6–8] However, there is an obstacle for practical applications because they require special readout equipment such as optical CT or MRI scanners.

Optical dosimetry using scintillating materials and camera systems is another viable candidate for two-dimensional (2D) and/or 3D dosimetry for radiation therapy beams; several papers on such dosimetry have been published for conventional x-ray radiation therapy, proton therapy, and carbon-ion therapy.[9–11] Recently, in a clinical BNCT facility, Yamamoto et al. and Yabe et al. reported the optical imaging of thermal neutron distribution and Cerenkov radiation distribution, which originated from 2.2 MeV gamma rays owing to the ^{1}H(n, γ)^{2}H reaction.[12,13] Motivated by these previous studies, we attempted direct optical observation of the boron-dose distribution using a ^{10}B-added liquid scintillator and a charge-coupled device (CCD) camera. We conducted a preliminary experiment using a thermal neutron beam at the E-3 port facility of the Kyoto University Research Reactor (KUR). The first optical

TABLE 1 Comparison of characteristics of neutron fields of E-3 port facility of KUR and those of typical accelerator based clinical BNCT facility.

	E-3 port facility of KUR	Typical accelerator based clinical BNCT facility
Thermal neutron flux	~ 1 x 10^5 n/cm^2/s	~ 1 x 10^9 n/cm^2/s
Spectral information of the beam	Almost pure thermal neutron	Epi-thermal neutron is dominant, including fast neutron.
Gamma-ray contamination	~ 1 μSv/h	~ 1 Gy/h

The thermal neutron flux in the E-3 port was measured by gold foil activation method when the reactor power was set to 1 MW in our previous experiment.

observation of the boron-dose distribution was successfully conducted under a neutron irradiation time of 600 s.[14]

It should be noted that the neutron field characteristics of the E-3 port facility are significantly different from those of a typical accelerator based clinical BNCT facility, as summarized in Table 1. In a clinical BNCT neutron field, a short irradiation time (approximately a few seconds) is sufficient to acquire clear images because of the intensive thermal neutron flux. However, there is a concern about the increase in unwanted luminescence that is not related to the boron dose, owing to recoil protons or gamma rays.

Kaplan et al. and Rosenfeld et al. have studied subtraction methods to eliminate the effects of gamma rays. In their method, a pair of dosimeters was used: the first one was covered by a ^{10}B converter, and the other was a bare dosimeter.[15,16] Similar to their studies, we assumed that the unwanted luminescence mentioned above could be eliminated through the subtraction method using liquid scintillators with and without ^{10}B. In this study, we experimentally investigated the feasibility of our optical imaging method for boron-dose distribution using a boron-added liquid scintillator and a CCD camera in a clinical BNCT neutron field.

2 | MATERIALS AND METHODS

The irradiation experiment was conducted at the Kansai BNCT Medical Center, which has an accelerator-based BNCT system (NeuCure, Sumitomo Heavy Industry Co., Tokyo, Japan) developed based on a cyclotron-based neutron source (C-BENS).[17] In this BNCT system, fast neutrons generated by the proton beams at the beryllium target were moderated to epi-thermal neutrons using a moderator system composed of Fe, Pb, Al, and CaF_2. The epi-thermal neutron beam was then shaped by a collimator made of polyethylene containing natural LiF. Tanaka et al. reported details of the moderator, collimator, and energy spectrum of the epi-thermal neutron beam.[17]

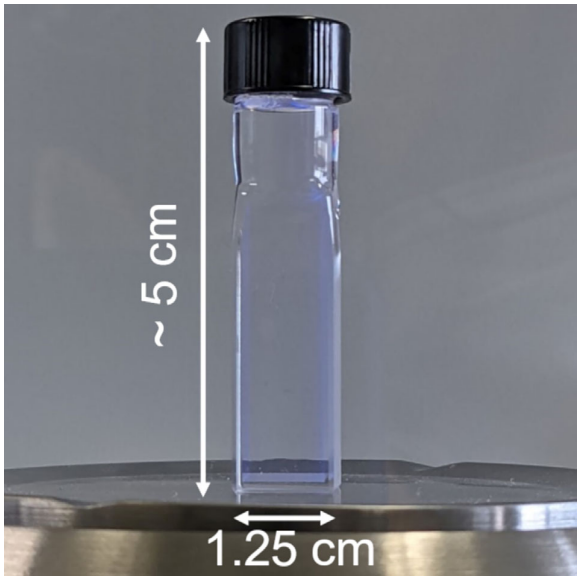

FIGURE 1 A picture of the liquid scintillator phantom that contains 1 wt% of natural boron.

2.1 | Phantom preparation and camera system

In this study, a quartz glass container filled with a liquid scintillator was used, as shown in Figure 1. Hereinafter, we refer to a glass container that is filled with liquid scintillator as "phantom." Based on our previous study,[14] we prepared two types of phantoms with and without ^{10}B by filling glass containers with a commercially available liquid scintillator (Insta-Gel Plus, Perkin Elmer, USA) and trimethyl borate. The natural boron concentrations were 1 and 0 wt%, respectively. Based on the natural abundance of ^{10}B, a natural boron concentration of 1 wt% was equivalent to 2000 ppm (μg/g) of ^{10}B concentration. The outer dimensions of the cross section of the quartz glass container were 1.25 cm $\times$ 1.25 cm and the thickness of the glass wall was 1.25 mm; the inner dimensions of the container were 1 cm $\times$ 1 cm. The height of the container, including its cap, was approximately 5 cm.

The camera system used was the same as that used in our previous paper[14]: a cooled CCD camera (SBIG-8300 M, SBIG, California, USA) with a 16-bit monochrome image sensor and an optical lens with an f-number of 0.95 (Xenon25 F/0.95, Schneider, Germany). The camera was cooled to −5°C during the experiment to suppress dark current noise and operated in a pixel binning mode of 5 $\times$ 5, such that the resolution of the

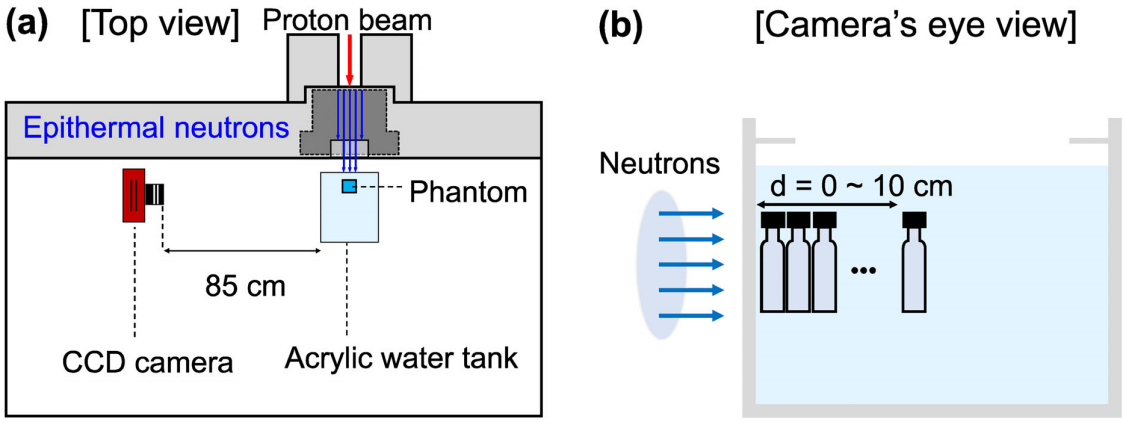

FIGURE 2 Schematic drawings of the instrument setup in the experiment: top view (a) and camera's eye view (b). The treatment couch and shielding materials for the CCD camera are omitted in Figure 2(a).

images was 670 × 506 pixels. The size of a single pixel of the images was 1.04 mm × 1.04 mm.

2.2 | Experimental setup and imaging of phantoms

First, the ^{10}B-added phantom (1 wt%) was placed in an acrylic water tank filled with pure water, which was placed on the treatment couch, as shown in Figure 2a. The outer dimensions of the water tank were 25 cm (W) × 25 cm (D) × 35 cm (H), and the thickness of each wall was 4 mm. The neutron beam was collimated to a diameter of 10 cm before irradiating the acrylic water tank. The entire system was covered with a light-shielding sheet to remove stray light from the treatment room. The camera was remotely controlled using a laptop computer installed in the next room through a 10 m USB cable.

As shown in Figure 2b, optical images were acquired at each position while the phantom was manually moved along the beam axis in 1 cm increments from 0 to 10 cm of *d*, where *d* denotes the nominal distance from the inner side of the tank wall to the surface of the phantom. Each irradiation time of neutron beam was approximately 2 s, and the exposure time of the CCD camera was set to 30 s to ensure sufficient coverage of the irradiation time. Blank images were also acquired to correct for the dark-current noise of the CCD elements at each position for the same exposure time. All images of the 1 wt% phantom and blank images were acquired once at each phantom position.

Thereafter, the phantom without ^{10}B (0 wt%) was placed in the tank, and images of the 0 wt% phantom and the corresponding blank images were taken in the same manner at each position. The total neutron irradiation time, including those of the other experiments, was approximately 1 min.

In this experiment, the camera was protected from the scattered thermal neutrons in the treatment room

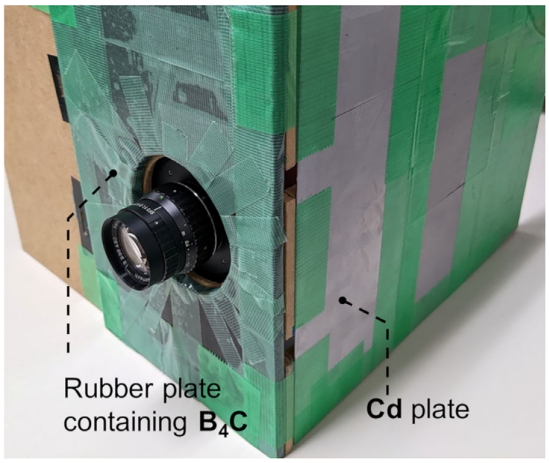

FIGURE 3 A picture of the arrangement of the shielding materials for the CCD camera from scattered neutrons. These shielding materials were bonded to medium density fiberboards (MDF) and combined at a perpendicular angle.

to prevent potential damage by incident neutrons. The front side of the camera was shielded using a rubber plate containing B_4C with a viewing hole. A side of the camera on the neutron-source side was covered with a cadmium plate; a cadmium plate with a thickness of 1 mm in the close vicinity of the camera and a thickness of 0.5 mm elsewhere was used. The arrangement of the shielding materials is shown in Figure 3. The method used for evaluating radiation damage to the camera is described below.

2.3 | Image processing

All images were analyzed using public-domain software (ImageJ, ver. 1.53e). Salt-and-pepper noise was removed using "Remove Outliers" function, a built-in function of ImageJ, with default settings. Blank images

were subtracted from those captured during the neutron irradiation at the corresponding depth of each phantom. Subsequently, these subtracted images were normalized to the beam charges of the protons, which were collected by a transmission ion chamber. The beam charges corresponded to the monitor unit in conventional radiotherapy. This was because there was some fluctuation in the proton beam charge owing to the very short irradiation time of a few seconds. Thereafter, we subtracted the images of the 0 wt% phantom from those of the 1 wt% phantom to eliminate luminescence irrespective of the boron dose.

For each processed image, a region of interest (ROI) was set in the central part of the phantom, and the average pixel value in the ROI was acquired. The dimensions of the ROI were 5 × 10 pixels (equivalent to approximately 0.5 cm × 1.0 cm). Finally, we obtained a depth profile consisting of 11 discrete points from the subtracted images corresponding to the depths of the phantoms. This resulted in a spatial resolution of 1 cm for this depth profile; the inner width of the phantoms was 1 cm, and the phantoms were moved in 1 cm increments. This depth profile was compared with that of the calculated boron dose and the depth profiles of the thermal neutron flux experimentally measured by the activation method with a gold wire or calculated using the Monte Carlo code, as described below.

2.4 | Monte Carlo simulation

To calculate the boron-dose and thermal neutron flux distributions, Monte Carlo simulations were performed using the particle and heavy-ion transport code system (PHITS, ver. 3.28).[18–20] We constructed the geometry based on the experimental setup: an acrylic water tank and a 1 wt% phantom were arranged in it, as shown in Figure 4. In this simulation, we omitted the shielding materials for the camera, B_4C rubber and Cd plates. This was because they were located approximately 85 cm from the surface of the water tank and did not affect the simulation results. Therefore, we simulated only the water tank and the phantom. In addition, we assumed that the emitted light would reach the camera directly. In short, we did not consider other behaviors of the emitted visible light, such as scattering, refraction, and reflection. For simplicity, a parallel neutron beam with a diameter of 10 cm was irradiated onto the phantom through the water tank entrance wall. The neutron energy spectrum of the C-BENS was used for this simulation.[17] The elemental composition of the Insta-Gel Plus was obtained from the application note provided by PerkinElmer Inc.[21]

First, we calculated the thermal neutron flux distribution in the water tank without phantoms. The validity of the calculation was verified by comparing the calculated depth profile of the thermal neutron flux with that measured using the activation method with a gold wire. It should be noted that the depth profile of the thermal neutron flux is measured using only the gold activation method in conventional QA. Both the depth profiles obtained by the calculation and measurement were free from ^{10}B perturbation because the boron-containing phantoms were not placed in the water tank.

Second, we calculated the mean boron dose in the ROI of the 1 wt% phantom at each depth in the water tank. We then obtained a discrete depth profile for the boron dose by following the same procedure as that used in the experiment. This calculation was performed to verify that the discrete depth profile of the boron dose calculated above was consistent with that of the thermal neutron flux calculated in the water tank without any phantoms. We also calculated the thermal neutron flux distribution around the position of 1 wt% phantom at a depth of 1 cm to determine how the thermal neutron flux was perturbed by the 1 wt% phantom with ^{10}B.

Third, assuming that the acrylic water tank was completely filled with a liquid scintillator with a natural boron concentration of 1 wt%, the thermal neutron flux in the scintillator-filled tank was calculated. This calculation was performed to predict neutron perturbations when an extremely large container was used to capture a larger area with a single shot using a CCD camera.

Finally, we calculated the mean deposited dose by secondary gamma rays, for example, 2.2 MeV gamma rays from $^1H(n,\gamma)^2H$, in the ROI of the 0 wt% phantom at each depth. In this study, a subtraction method was used to remove the luminescence component irrespective of the boron dose. Therefore, the lower luminescence of the 0 wt% phantom was preferable because it was the background luminescence that should be subtracted from the luminescence of the 1 wt% phantom. This calculation was performed to determine the origin of the luminescence of the 0 wt% phantom.

The calculation of the boron dose was performed through the “e–mode” and T–deposit tallies, whereas the thermal neutron flux was scored using the T–track tally. To precisely consider the behavior of thermal neutrons, a built-in thermal scattering law data $S(\alpha,\beta)$ library was used. Considering that the major component of Insta-Gel Plus is pseudocumene, which is similar to the benzene ring, the $S(\alpha,\beta)$ data of the benzene ring were substituted for those of Insta-Gel Plus. The statistical uncertainty was less than 2% for the boron dose at a depth of 2 cm, and less than 1% for the thermal neutron flux over the entire water tank.

2.5 | Damage assessment of the CCD camera by neutrons

It is necessary to evaluate the radiation damage to the CCD camera when the camera is used in an intensive

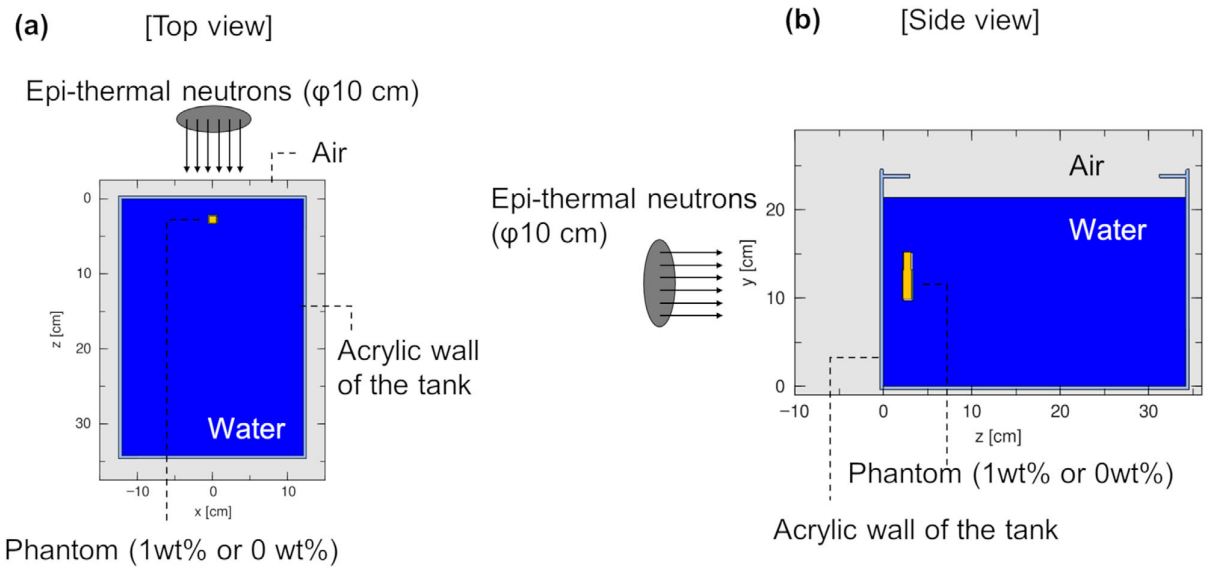

FIGURE 4 Examples of the geometry of the Monte Carlo simulation for a phantom position of $d = 2$ cm: top view (a) and side view (b).

neutron field, because the CCD elements are probably damaged. Yamamoto et al. reported that their CCD camera without neutron shielding was slightly damaged by scattered neutrons in the BNCT treatment room.[12] They stated that the number of white spots with high intensity increased by approximately a factor of four; such white spots were permanent and did not decrease with time.

We assessed the damage to the CCD camera caused by the neutrons based on the number of permanent white spots in the dark frame images observed in a dark box. Before the neutron irradiation experiment, dark frame images were captured in the dark box, enabling the dark frame mode, twice on separate days. Ten dark frame images were taken with an exposure time of 30 s per day, that is, 20 images in total. The camera operating parameters, cooling temperature, and binning settings, were identical to those used in the neutron irradiation experiments. We defined CCD elements with pixel values above a certain threshold in all 20 dark-frame images as permanent white spots. According to the criteria described in the paper of Pugliesi et al.,[22] we set the threshold pixel value at 6000 in this study in such a way that the proportion of permanent white spots was approximately 0.1% of the total pixels of these images before the irradiation. Based on this threshold, permanent white spots were extracted and counted prior to neutron irradiation. Two weeks after the neutron irradiation experiment, 20 dark-frame images were captured, and the permanent white spots were counted in the same manner. Thereafter, we assessed the damage to the CCD camera caused by neutrons based on the increasing number of permanent white spots.

3 | RESULTS

3.1 | Acquired images and depth profiles

The images of the 1 wt% phantom, 0 wt% phantom, and the subtracted images between them for some depths, d, are shown in Figure 5. Artifacts appeared in the images at a depth d of 0 cm, which were reflections of the tank wall on the left side of the phantom. As a result of subtraction, only the boron dose components were successfully extracted as subtracted images at each depth d. Figure 6 shows the discrete depth profiles of the pixel values obtained from these images. All profiles reached a peak at a depth of approximately 2 cm and subsequently decayed gradually with increasing depth, whereas that of the 0 wt% phantom decreased more gradually with increasing depth than those of the others.

The depth profiles of the subtracted images, calculated boron dose at each position of the phantom, calculated thermal neutron flux, and experimentally obtained thermal neutron flux using gold wire are shown in Figure 7. The four curves were normalized to their maximum values. The depth profile of the calculated thermal neutron flux in the water tank generally agreed with that measured using the gold wire. Furthermore, the depth profile of the subtracted image was in good agreement with the calculated boron dose and thermal neutron flux distributions in the water tank, except at a depth of approximately 1 cm. The relative difference between the experimental profile and the calculated boron-dose profile was less than 4 % up to a depth of 6 cm, except for at depth of approximately 1 cm, where there was approximately 14% difference, and less than 10% difference for a depth larger than 6 cm.

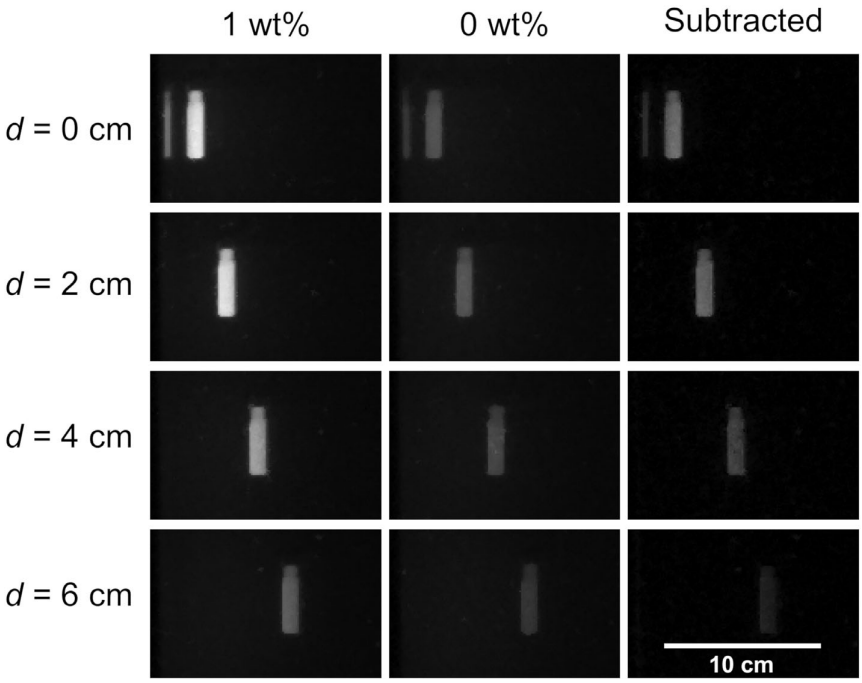

FIGURE 5 Example images of the 1 wt% phantom, 0 wt% phantom, and subtracted images between them for some depths *d*.

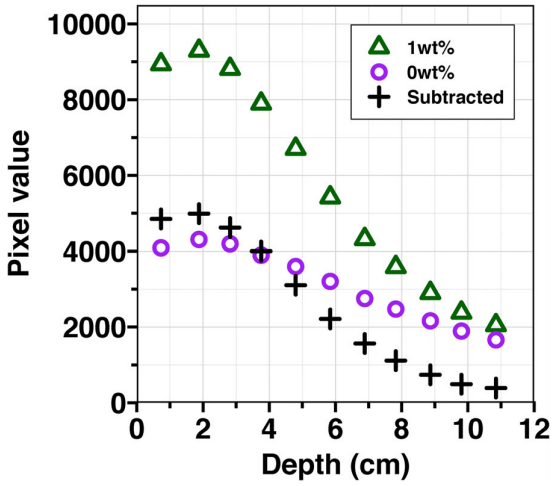

FIGURE 6 Discrete depth profiles of pixel values obtained from the images in Figure 5.

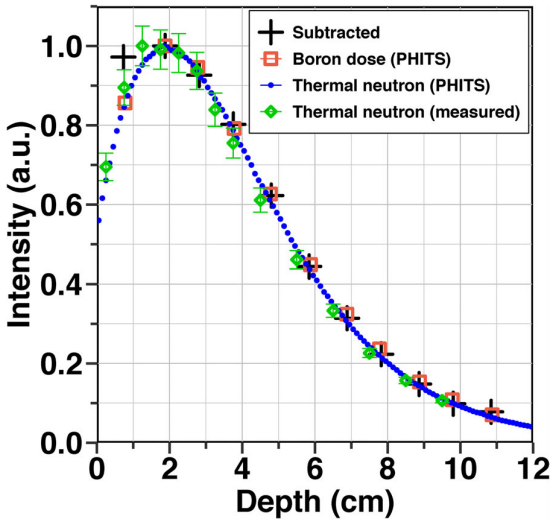

FIGURE 7 The depth profile of the subtracted images, the depth profile of calculated boron dose at each position of the phantom, the depth profile of calculated thermal neutron flux, and the depth profile of the experimentally measured thermal neutron flux by gold wire.

3.2 | Perturbation of thermal neutron flux distribution by the existence of ^{10}B-containing liquid scintillator

Figure 8 shows the horizontal cross-sectional view of the calculated thermal neutron flux distributions when the ^{10}B-containing phantom was not placed in the water tank (a), when the 1 wt% phantom was placed at d = 1 cm in the water tank (b), and when the acrylic tank was entirely filled with a liquid scintillator with a natural boron concentration of 1 % (c). Obviously, in Figure 8a, the thermal neutron flux distribution in the water tank is free from the perturbation effect of the ^{10}B-containing phantom. As shown in Figure 8b, even when a relatively small 1 wt% phantom was used, the neutron perturbation was not negligible. When the acrylic tank is entirely filled with 1 wt% liquid scintillator, the trend

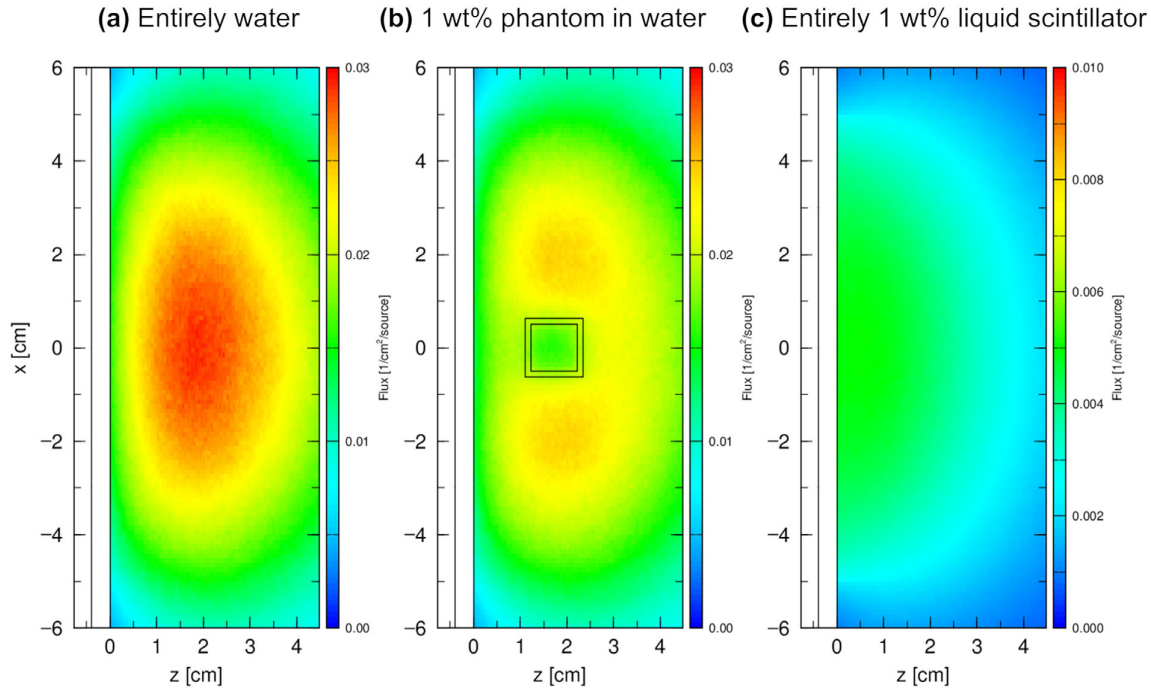

FIGURE 8 Calculated thermal neutron flux distributions [cross sectional view] (a) the phantom is not in the water tank, (b) the 1 wt% phantom is placed at $d = 1$ cm, and (c) the entire tank is filled with liquid scintillator with a natural boron concentration of 1 wt%; due to quite low thermal neutron flux in (c), this image is displayed with the different color scale from other images.

may be more significant, as shown in Figure 8c for an extreme case. Despite this non-negligible perturbation of the ^{10}B-containing liquid scintillator shown in Figure 8, the experimental depth profile showed good agreement with the depth profiles of the calculated boron dose and thermal neutron flux distributions, as shown in Figure 7.

3.3 | Deposited energy to 0 wt% phantom by secondary gamma rays

The measured discrete depth profile of the pixel values of the 0 wt% phantom (the same data as in Figure 6) and the calculated depth profile of the gamma-ray dose at each position of the phantom are compared in Figure 9. The profiles were normalized to their maximum values. In this figure, these depth profiles show similar overall trends, although there are some non-negligible discrepancies. In the region deeper than approximately 7 cm, the depth profile of the 0 wt% phantom showed a more moderate decrease with an increase in depth than that of the calculated gamma-ray dose profile.

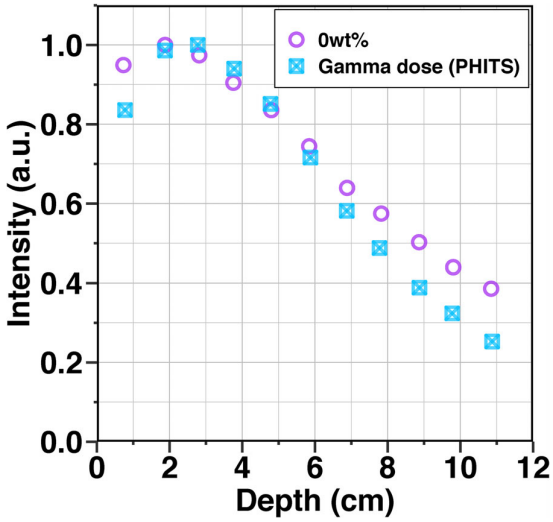

FIGURE 9 Comparison of the experimental depth profile of the 0 wt% phantom and the calculated depth profile of the gamma-ray dose in the 0 wt% phantom. These profiles are normalized to their maximum values.

3.4 | Water luminescence accompanied by a neutron incident

In the shallow region of the water tank, relatively weak luminescence of water was also commonly observed under the 1 and 0 wt% phantom conditions. An image of the 0 wt% phantom at $d = 10$ cm is shown in Figure 10 as an example. Figure 11 shows the observed depth profiles along the beam axis of the images when the 1 wt % and 0 wt% phantoms were placed at $d = 2$,

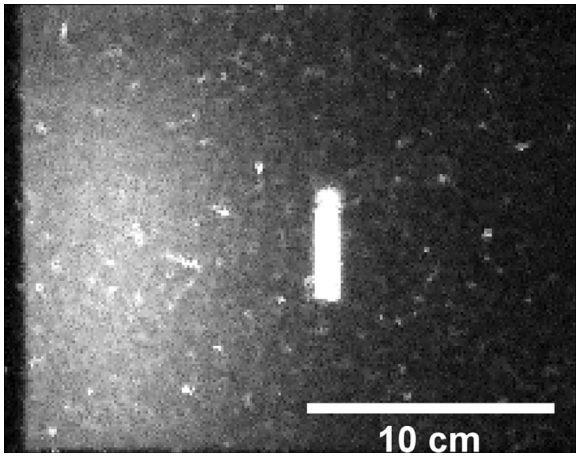

FIGURE 10 An example of observed water luminescence in the shallow region [Left side part]. Gray scale level is adjusted to emphasize the weak luminescence from water in the tank.

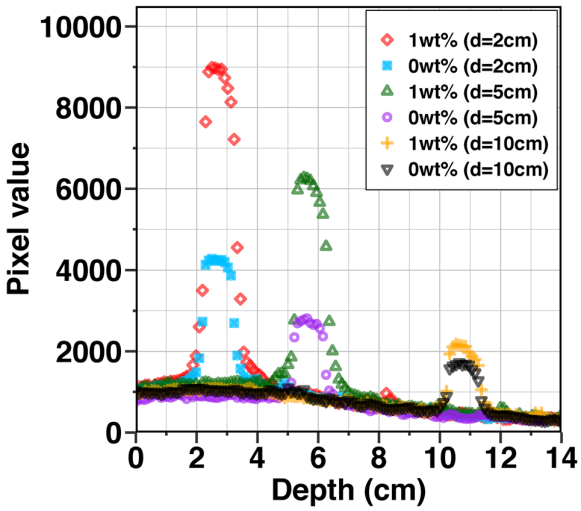

FIGURE 11 Observed depth profiles along the beam axis of the images when 1 wt% and 0 wt% phantoms were placed at $d = 2, 5,$ and 10 cm.

5, and 10 cm, respectively. These six profiles exhibit almost the same behavior in the water region owing to their relatively weak luminescence. This luminescence decreased gradually with increasing depth up to 14 cm, except for the three peak regions around the phantoms. In all images, such water luminescence was similarly observed, independent of the boron concentration and the nominal depth of the phantoms.

3.5 | Damage assessment of the CCD camera by neutrons

Examples of dark-frame images captured before and after neutron irradiation experiments are shown in Figure 12. Using 20 blank images, we evaluated the frequency distributions of the pixel values before and after the neutron irradiation experiment. The resulting histograms of the pixel values are shown in Figure 13. Based on Figure 13, the threshold pixel value was determined to be 6000 and permanent white spots that commonly appeared in all 20 blank images were extracted. There were 373 permanent white spots before irradiation (a) and 408 after irradiation (b).

4 | DISCUSSION

4.1 | Validity of the subtraction method using the small phantoms with and without ^{10}B

As shown in Figure 7, the profile of the calculated boron dose corresponds well with the depth profiles of the thermal neutron flux. The profile of the pixel values obtained from the subtracted images in Figure 5 is in good agreement with the calculated results mentioned above, except in the shallow region where the depth is approximately 1 cm. This discrepancy was mainly owing to the influence of the artifact of the reflected light on the tank wall, as mentioned in the explanation of Figure 5. Such artifacts can be suppressed using a special water tank with a black wall. In this case, the subtracted images correctly expressed the boron dose. Therefore, a subtraction method based on scanning a small phantom is valid for boron-dose distribution measurements.

4.2 | Background luminescence of the 0 wt% phantom

The origin of the luminescence observed for the 0 wt% phantom is discussed below, because such luminescence is the background that should be properly subtracted as a noise component to evaluate the boron dose; the poor S/N ratio causes inaccurate boron-dose determination. As illustrated in Figure 6, the pixel value of the images of the 0 wt% phantom was almost half of that of the 1 wt% phantom, where d was 2 cm. In contrast, in our preliminary experiments at the E-3 port of KUR, the luminescence of the 0 wt% phantom was less than 2 % of that of the 1 wt% phantom.[14] We assumed that the major origin of the present high background luminescence might be the presence of water around the phantom. Owing to ^{1}H(n, γ)^{2}H reaction, 2.2 MeV gamma rays with a long mean free path are generated. The liquid scintillator is sensitive not only to the charged particles generated by the boron neutron capture reaction, that is, ^{7}Li nuclei and alpha particles, but also to gamma rays. The number of such gamma rays reaching the phantom from outside the phantom would be significantly greater than that of ^{7}Li nuclei and alpha particles

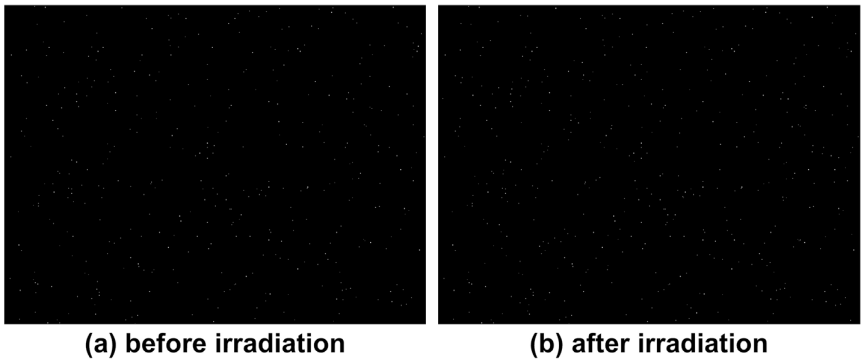

FIGURE 12 Examples of the dark frame images taken before (a) and after (b) the neutron irradiation experiment.

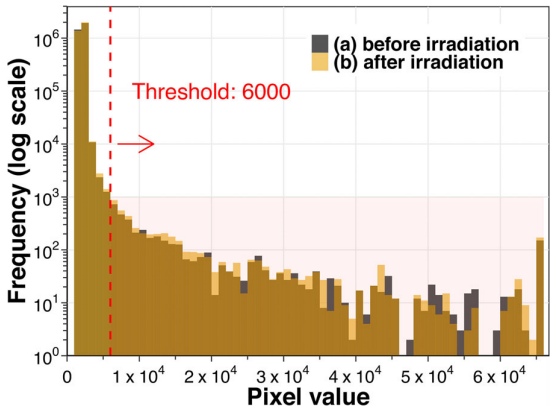

FIGURE 13 Histograms of the frequency of pixel values in 20 blank images before (a) and after (b) the neutron irradiation experiment.

emitted inside the phantom, when a considerably large neutron beam diameter of 10 cm and a large volume of water surrounding the phantom were considered. As shown in Figure 9, the depth profiles of the 0 wt% phantom and the calculated gamma-ray dose showed similar trends. This finding partially supports our assumption.

However, the depth profile of the 0 wt% phantom in Figure 9 shows some discrepancies from that of the secondary gamma-ray dose depth profile, both in the shallow region where the depth is approximately 1 cm and in the region deeper than approximately 7 cm. The discrepancy in the shallow region may be related to light reflected from the tank wall, as described above. Here, we note a discrepancy in the deep regions. One possible reason for this discrepancy is the contribution of the water luminescence, as shown in Figure 10. This luminescence is thought to be due to Cerenkov light as reported by Yabe et al.[13] Figure 11 illustrates that approximately 30 % of the total pixel values of the 0 wt% phantom observed around the three peaks may be due to the contribution of Cerenkov light generated in the surrounding water. Usually, Cerenkov light is far weaker than the scintillation light; however, it can be detected as a certain signal because the volume of water irradiated with neutrons is larger than that of the scintillator, as previously mentioned. Therefore, the observed images of the 0 wt% phantom contained both the scintillation light emitted from the liquid scintillator in the phantom and the Cerenkov light emitted from the water surrounding the phantom. Unfortunately, the Monte Carlo code used in this study (PHITS) could not simulate Cerenkov light emission. We believe that this contribution of the Cerenkov light explains why the depth profile of the 0 wt% phantom cannot be explained by the secondary gamma-ray dose alone.

4.3 | Points to be improved

In this study, the potential of the optical observation method for the boron dose was verified in a clinical BNCT field. However, the method used in this experiment was still time-consuming, similar to conventional scanning methods using point detectors, such as ionization chambers. In addition, the obtained spatial resolution of the boron-dose distribution was 1 cm, which is not sufficient for a modern QA method. To prove the principle, we used a scanning method with a small phantom, because large quartz glass containers were not available. If a larger quartz glass container were available, a wider area could be observed with a better spatial resolution in a single shot. An acrylic container that is resistant to liquid scintillators would be a solution to these problems, because there have been several studies in which liquid scintillators were sealed in acrylic containers for photon or proton therapy dosimetry.[23–25] When using such large acrylic containers for BNCT dosimetry, two issues should be considered, as discussed in the following sections: (a) the thermal neutrons are perturbed by the ^{10}B-containing phantom, and (b) the boron-dose distribution cannot be directly evaluated in detail from the obtained images owing to the projection (or integration) effect along the optical axis of the camera.

4.4 | Perturbation effect of the ^{10}B-containing liquid scintillator

As shown in Figure 8a and 8b, the thermal neutron flux perturbation of the 1 wt% phantom cannot be completely ignored, even when a relatively small phantom is used. A natural boron concentration of 1 wt% corresponds to a very high concentration of 2000 ppm in terms of ^{10}B concentration (in clinical applications, approximately 25 ppm is the nominal concentration of ^{10}B in the blood). As a result, the mean free path of the thermal neutrons in the 1 wt% phantom was much shorter than that in water. Nevertheless, if the container of the phantom is sufficiently small, as in this study, the relative boron dose distribution is still observable because the perturbation effect is moderated by scattered thermal neutrons from the surrounding water. On the other hand, as shown in Figure 8c, if a considerably large acrylic container with the same boron concentration is used, the thermal neutron flux distribution in the container is significantly disturbed because there is no surrounding water. In this case, the depth profile evaluated from the obtained images would be quite different from the profile of the thermal neutron flux measured using the conventional gold activation method.

A straightforward reduction in boron concentration can suppress this perturbation; however, it also decreases the sensitivity to the boron dose. Therefore, there is a critical trade-off between the low perturbation of the thermal neutron flux and the high sensitivity of boron-dose detection. Careful selection of boron concentration is essential when using larger containers.

4.5 | Projection effect along the optical axis

When the emitted light distribution in the 3D space is projected onto 2D images, the pixel values of the CCD elements are approximately equal to the line integration of the light distribution along the optical axis. If a large container is used, this projection effect is significant; the obtained images reflect the overall dose distribution in the container, and a precise evaluation of the local dose distribution becomes difficult. Some reconstruction techniques are required to evaluate the 3D dose distribution; however, they typically require multiple projected images from different angles.[26] Usually, such an approach complicates the procedure.

4.6 | Future plans

As stated above, simply enlarging the container dimensions with 1 wt% natural boron may yield poor results. We plan to apply a straw-like narrow glass tube as a container filled with liquid scintillators set along the beam axis to reduce the perturbation and projection effects to practically acceptable levels. If this method can be successfully realized, we will be able to observe a wide area at once with a spatial resolution of approximately 1 mm while keeping the ^{10}B concentration of the phantom unchanged. We expect that this spatial resolution of 1 mm is the best possible resolution for the proposed method with the camera system used in this study because it corresponds to the pixel size of the images. A finer spatial resolution can be achieved using a camera system with a higher resolution and sensitivity.

4.7 | Damage assessment of the CCD camera

As stated in Section 3.5 **"**Damage assessment of the CCD camera by neutrons," the number of permanent white spots on the CCD camera increased by approximately 10% from 373 to 408 owing to the neutron irradiation experiment. Yamamoto et al. studied the damage to the CCD camera during similar neutron irradiation experiments without particular neutron shielding.[12] We prepared neutron shielding as previously mentioned in this study. However, we cannot discuss the effect of neutron shielding because a direct comparison is not possible between the results of Yamamoto et al. and those obtained in this study for the following reasons. First, the distance between the camera and water tank used was different. Second, the CCD cameras used were different; therefore, the vulnerabilities of the CCD elements were different. In addition, the details of the analysis procedure for permanent white spots were not described by Yamamoto et al. Therefore, it is likely that the definitions of permanent white spots differ. Nevertheless, as far as the results obtained in this study are concerned, we may conclude that an increase of relatively 10% in permanent white spots is acceptable for practical use when appropriate neutron shielding is prepared. This is because the absolute increased number of white spots corresponds to only 0.01% of the total pixel number of the CCD element used for the present study.

5 | LIMITATIONS

This study had several limitations. First, the information obtained by the present method is only the relative boron-dose distribution, whereas the gold activation method provides thermal neutron flux information by which the absolute boron dose can be evaluated by calculation. Second, the phantoms used in this study were not optimized in terms of their boron concentrations or dimensions, which yielded the insufficient spatial resolution of the depth profile. Third, we did not confirm the reproducibility of the proposed method and the

linearity between the pixel values of the images and the boron dose. Finally, as stated in the "2.4 Monte Carlo simulation," we ignored the contributions of reflection, refraction, and scattering of emitted visible light. Our simulation could not explain the partial discrepancy between the depth profile of the subtracted images and the calculated depth profile of the boron dose in the shallow region.

6 | CONCLUSION

The validity of the newly proposed boron-dose evaluation method using phantoms with and without ^{10}B was experimentally confirmed in the neutron field of an accelerator-based BNCT clinical facility, although some issues remained to be resolved. The effects of the measurement parameters, such as the dimensions of the liquid scintillator container and boron concentration, were examined. The origins of the background signals were also discussed. Finally, the limitations of the proposed method were summarized. The most critical point to be improved is the trade-off between the luminescence intensity of the phantom with ^{10}B and its perturbation effect on the thermal neutron flux, which depends on both the dimensions of the liquid scintillator container and the boron concentration. Further studies are needed to establish a more practical evaluation method for the boron-dose distribution.

ACKNOWLEDGMENTS

This study was partly supported by JSPS KAKENHI (grant numbers JP19K08202 and JP22K07697).

CONFLICT OF INTEREST STATEMENT

The authors have no conflicts to disclose.

DATA AVAILABILITY STATEMENT

There is no usable data to share.

REFERENCES

1. Locher G. Biological effects and therapeutic possibilities of neutrons. *AJR Am J Roentgenol*. 1936;36:1-13.
2. Hirose K, Kato T, Harada T, et al. Determining a methodology of dosimetric quality assurance for commercially available accelerator-based boron neutron capture therapy system. *J Radiat Res*. 2022;63(4):620-635. doi:10.1093/jrr/rrac030
3. Kobayashi T, Sakurai Y, Ishikawa M. A noninvasive dose estimation system for clinical BNCT based on PG-SPECT-Conceptual Study and fundamental experiments using hpge and CdTe semiconductor detectors. *Med Phys*. 2000;27(9):2124-2132. doi:10.1118/1.1288243
4. Okazaki K, Tanaka H, Takata T, Kawabata S, Akabori K, Sakurai Y. Evaluation of the energy resolution of a prompt gamma-ray imaging detector using LaBr3(CE) scintillator and 8 × 8 array MPPC for an animal study of BNCT. *Appl Radiat Isot*. 2020;163:109214. doi:10.1016/j.apradiso.2020.109214
5. Murata I, Kusaka S, Minami K, et al. Design of SPECT for BNCT to measure local boron dose with Gagg scintillator. *Appl Radiat Isot*. 2022;181:110056. doi:10.1016/j.apradiso.2021.110056
6. Khajeali A, Farajollahi AR, Khodadadi R, Kasesaz Y, Khalili A. Role of gel dosimeters in boron neutron capture therapy. *Appl Radiat Isot*. 2015;103:72-81. doi:10.1016/j.apradiso.2015.05.017
7. Gambarini G, Artuso E, Giove D, et al. Study of suitability of Fricke-gel-layer dosimeters for in-air measurements to characterise epithermal/thermal neutron beams for NCT. *Appl Radiat Isot*. 2015;106:145-150. doi:10.1016/j.apradiso.2015.07.036
8. Tanaka K, Kajimoto T, Mitsuyasu A, et al. Measurement of spatial fluence distribution of neutrons and gamma rays using Magat-type gel detector doped with LiCl for BNCT at Kyoto University Reactor. *J Phys Conf Ser*. 2022;2167(1):012006. doi:10.1088/1742-6596/2167/1/012006
9. Rilling M, Allain G, Thibault S, Archambault L. Tomographic-based 3D scintillation dosimetry using a three-view Plenoptic Imaging System. *Med Phys*. 2020;47(8):3636-3646. doi:10.1002/mp.14213
10. Beddar S, Archambault L, Sahoo N, et al. Exploration of the potential of liquid scintillators for real-time 3D dosimetry of intensity modulated proton beams. *Med Phys*. 2009;36(5):1736-1743. doi:10.1118/1.3117583
11. Tamborini A, Raffaele L, Mirandola A, et al. Development and characterization of a 2D scintillation detector for quality assurance in scanned carbon ion beams. *Nucl Instrum Methods Phys Res A*. 2016;815:23-30. doi:10.1016/j.nima.2016.01.040
12. Yamamoto S, Yabe T, Hu N, Kanai Y, Tanaka H, Ono K. Technical note: optical imaging of lithium-containing zinc sulfate plate in water during irradiation of neutrons from boron neutron capture therapy (BNCT) system. *Med Phys*. 2022;49(3):1822-1830. doi:10.1002/mp.15424
13. Yabe T, Yamamoto S, Hu N, Kanai Y, Tanaka H, Ono K. First measured optical image of Cerenkov-light in water during irradiation of neutron beam from boron neutron capture therapy (BNCT) system. *Radiat Meas*. 2021;146:106633. doi:10.1016/j.radmeas.2021.106633
14. Nohtomi A, Maeda H, Sakamoto N, Wakabayashi G, Takata T, Sakurai Y. First optical observation of 10B-neutron capture reactions using a boron-added liquid scintillator for quality assurance in boron neutron capture therapy. *Radiol Phys Technol*. 2022;15(1):37-44. doi:10.1007/s12194-021-00645-z
15. Rosenfled AB, Kaplan GI, Carolan MG, et al. Simultaneous macro and micro dosimetry with MOSFETs. *IEEE Trans Nucl Sci*. 1996;43(6):2693-2700. doi:10.1109/23.556855
16. Kaplan GI, Rosenfled AB, Allen BJ, Coderre JA, Liu HB. Fission converter and metal-oxide-semiconductor field effect transistor study of thermal neutron flux distribution in an epithermal neutron therapy beam. *Med Phys*. 1999;26(9):1989-1994. doi:10.1118/1.598703
17. Tanaka H, Sakurai Y, Suzuki M, et al. Characteristics comparison between a cyclotron-based neutron source and Kur-HWNIF for boron neutron capture therapy. *Nucl Instrum Methods Phys Res B*. 2009;267(11):1970-1977. doi:10.1016/j.nimb.2009.03.095
18. Sato T, Iwamoto Y, Hashimoto S, et al. Features of particle and heavy ion transport code system (PHITS). version 3.02. *J Nucl Sci Technol*. 2018;55(6):684-690. doi:10.1080/00223131.2017.1419890
19. Boudard A, Cugnon J, David J-C, Leray S, Mancusi D. New potentialities of the Liège intranuclear cascade model for reactions induced by nucleons and light charged particles. *Phys Rev C*. 2013;87(1):014606. doi:10.1103/PhysRevC.87.014606
20. Iida K, Kohama A, Oyamatsu K. Formula for proton–nucleus reaction cross section at intermediate energies and its application. *J Phys Soc Jpn*. 2007;76(4):044201. doi:10.1143/JPSJ.76.044201
21. PerkinElmer Inc. LSC in practice (LSC cocktails—elemental composition). Accessed February 24, https://resources.perkinelmer.com/lab-solutions/resources/docs/APP_LSCCocktailsElementalComposition.pdf 2023.
22. Pugliesi R, Andrade MLG, Dias MS, Siqueira PTD, Pereira MAS. Study of pixel damages in CCD cameras irradiated at the neutron

tomography facility of IPEN-CNEN/SP. *Nucl Instrum Methods Phys Res A*. 2015;804:59-63. doi:10.1016/j.nima.2015.09.067
23. Pönisch F, Archambault L, Briere TM, et al. Liquid scintillator for 2D dosimetry for high-energy photon beams. *Med Phys*. 2009;36(5):1478-1485. doi:10.1118/1.3106390
24. Darne CD, Alsanea F, Robertson DG, Sahoo N, Beddar S. Performance characterization of a 3D liquid scintillation detector for discrete spot scanning proton beam systems. *Phys Med Biol*. 2017;62(14):5652-5667. doi:10.1088/1361-6560/aa780b
25. Alsanea F, Darne C, Robertson D, Beddar S. Ionization quenching correction for a 3D scintillator detector exposed to scanning proton beams. *Phys Med Biol*. 2020;65(7). doi:10.1088/1361-6560/ab7876
26. Ashraf MR, Farwell C, Alexander DA, et al. 3D dose delivery QA using couch and gantry mounted cameras. *J Phys Conf Ser*. 2022;2167:012027. doi:10.1088/1742-6596/2167/1/012027

How to cite this article: Maeda H, Nohtomi A, Hu N, Kakino R, Akita K, Ono K. Feasibility study of optical imaging of the boron-dose distribution by a liquid scintillator in a clinical boron neutron capture therapy field. *Med Phys*. 2023;1-13. https://doi.org/10.1002/mp.16727